A TD-CIS study of high-harmonic generation of uracil cation fragments

Chiara Morassut, Eleonora Luppi, Emanuele Coccia

▶ **To cite this version:**

Chiara Morassut, Eleonora Luppi, Emanuele Coccia. A TD-CIS study of high-harmonic generation of uracil cation fragments. Chemical Physics, 2022, 559, pp.111515. 10.1016/j.chemphys.2022.111515 . hal-04023356

HAL Id: hal-04023356
https://hal.science/hal-04023356

Submitted on 10 Mar 2023

HAL is a multi-disciplinary open access archive for the deposit and dissemination of scientific research documents, whether they are published or not. The documents may come from teaching and research institutions in France or abroad, or from public or private research centers.

L'archive ouverte pluridisciplinaire **HAL**, est destinée au dépôt et à la diffusion de documents scientifiques de niveau recherche, publiés ou non, émanant des établissements d'enseignement et de recherche français ou étrangers, des laboratoires publics ou privés.

A TD-CIS study of high-harmonic generation of uracil cation fragments

Chiara Morassut

Dipartimento di Scienze Chimiche e Farmaceutiche, University of Trieste, via Giorgieri 1, 34127 Trieste, Italy

Eleonora Luppi

Sorbonne Universités, UPMC Univ Paris 06, UMR 7616, Laboratoire de Chimie Théorique, F-75005 Paris, France. CNRS, UMR 7616, Laboratoire de Chimie Théorique, F-75005 Paris, France

Emanuele Coccia

Dipartimento di Scienze Chimiche e Farmaceutiche, University of Trieste, via Giorgieri 1, 34127 Trieste, Italy

Abstract

High-harmonic generation (HHG) spectroscopy was investigated from laser ablation plasmas of uracil targets in the experimental work of Hutchinson *et al.*, [*Phys. Chem. Chem. Phys. Comparison of high-order harmonic generation in uracil and thymine ablation plumes*, 2013, **15**, 12308] and of Lopez-Quintas *et al.*, [*Appl. Surf. Sci., Characterization of laser-induced plasmas of nucleobases: Uracil and thymine*, 2014, **302**, 299]. Inspired by these works we computed HHG spectra of uracil cation fragments by means of real-time time-dependent configuration interaction with single excitations (RT-TD-CIS) and continuum-optimal Gaussian basis sets. We calculated the rotationally-averaged HHG spectra of different cation fragments analysing the relation between HHG, geometry of the fragments (linear/nonlinear) and electron dynamics (bound and continuum energy states). Moreover, to simulate the complexity of a sample containing fragments upon ablation, we calculated weighted-rotationally-averaged HHG spectra where the contribution of each fragment is included through weights assigned ac-

Email addresses: eleonora.luppi@sorbonne-universite.fr (Eleonora Luppi), ecoccia@units.it (Emanuele Coccia)

cordingly to the experimental mass spectra.

Keywords: nonlinear optics; quantum chemistry; ultrafast dynamics

1. Introduction

Attosecond atomic and molecular processes are nowadays intensively investigated thanks to the dramatic advances of ultrafast laser technology [1, 2, 3, 4, 5, 6, 7, 8]. Generation of attosecond pulses are indeed applied to study ultrafast electron dynamics in atomic and molecular systems with unprecedented time and spatial resolution [5, 9, 10, 11, 12].

Attosecond laser resolution is achieved by nonlinear optical processes, such as high-harmonic generation (HHG) [9, 10, 11, 12]. The HHG spectra are composed of the emitted harmonics of the infrared pulse frequency, from which one extracts information on the electronic structure and dynamical of the target [13, 14, 15, 16, 17, 18, 19, 20, 21, 22, 23, 24, 25, 26, 27, 28]. HHG spectra are used for molecular orbital tomography [14, 29, 30], to study interference among different electron channels characterising ionisation or recombination [31, 19, 18, 26], the role of quantum coherence [32], the ultrafast charge migration [33], and vibrational signatures emerging in the strong-field dynamics [34].

Application of HHG spectroscopy to organic and biological molecules presented some technical issues. [35] In fact, these molecules in ambient conditions are not easily volatile, and thus creating an high-density gas-phase sample is challenging. Innovative experimental works [36, 37] measured HHG spectra of uracil and thymine using laser ablation technique capable to produce plasma plumes from solid samples of the two nucleobases. The recorded signal originated from a complex relation between single-fragment features, phase matching and interaction among fragments [36, 37].

Theory helps the interpretation of the HHG measurements in complex molecular systems and time-resolved ab initio methods demonstrated to be successfully in this context. [24, 25, 38, 26, 39, 40, 41, 42, 43, 44, 45, 46, 47, 48, 49, 50, 51, 52].

Recently, some of us studied the rotational-averaged HHG spectra of uracil and thymine [51] within real-time time-dependent configuration interaction with single excitations (RT-TD-CIS) and continuum-optimal Gaussian basis sets. We developed this theoretical strategy for HHG in the recent years. [42, 43, 44, 45, 46, 51, 52] This approach represents a reasonable compromise between accuracy and computational cost, which permits an affordable treatment of many-electron systems interacting with strong fields.

Moreover, this approach allows one to control and systematically improve Gaussian basis sets.

Using the same theoretical approach, in this work our goal is computing and analysing the HHG spectra of the uracil cation fragments, in order to unravel the contribution of the single fragment in the plumes. [36, 37] Since Hutchinson *et al.* [36] and Lopez-Quintas *et al.* [37] do not give a fully molecular interpretation of the mass spectra, we used the fragmentation study of Arani *et al.* [53] for getting the molecular moieties for the HHG simulations. We calculated the rotationally-averaged HHG spectra of different cation fragments analysing the correlation between the shape of an HHG spectrum and the geometry of the fragments (linear/nonlinear) together with the electron dynamics (bound and continuum energy states). Moreover, to simulate the complexity of a sample containing a certain number of fragments after ablation, we calculated a weighted-rotationally-averaged HHG where the contribution of each fragments is included. The weights have been assigned accordingly to the measured peak heights in the experimental mass spectrum in Refs [36, 37].

The article is organised as follows: in Section 2 the theoretical framework for computing the HHG spectra is reviewed, computational details of our simulations are given in Section 3, and the results are presented and discussed in Section 4, while in Section 5, we summarize the main achievements of the present work and give perspectives for future developments.

2. Theory

2.1. Real-Time Time-Dependent Configuration-Interaction Singles (RT-TD-CIS)

In RT-TD-CIS, the time-dependent electronic wave function is written as

$$|\Psi(t)\rangle = \sum_{k\geq 0} c_k(t)|\Psi_k\rangle, \tag{1}$$

where $|\Psi_k\rangle$ for k=0 is the Hartree-Fock ground state $|\Psi_0\rangle$. For $k > 0$ we use the field-free (time-independent) CIS excited states, i.e. $|\Psi_k\rangle = \sum_{ia} d^a_{i,k}|\Phi^a_i\rangle$, constructed on singly-excited Slater determinants $|\Phi^a_i\rangle$, with an electron moving from the occupied molecular orbital i to the virtual one a, while $d^a_{i,k}$ are the linear coefficients. [54] The $c_k(t)$ represents the expansion coefficients that are time dependent and thus responsible for the time dependence in RT-TD-CIS. [41, 55]

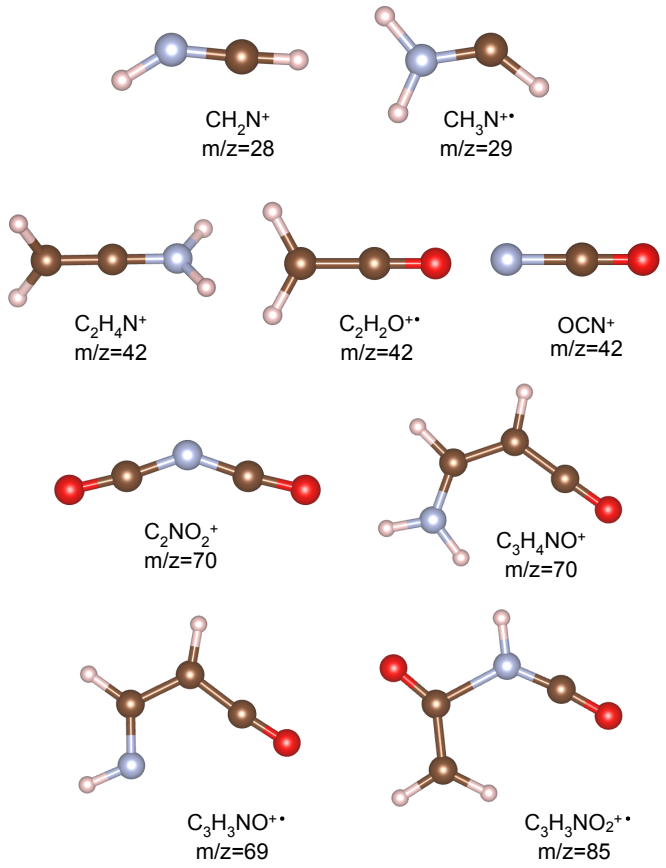

Figure 1: Fragments of the uracil cation and mass/charge (m/z) ratio. O atoms are red, C atoms are brown, N atoms are grey and H atoms are white.

The time-dependent Schrödinger equation (TDSE) for the coefficients $c_k(t)$ is (atomic units) [42, 43, 44, 45, 46, 51]

$$i\frac{\partial c_k(t)}{\partial t} = \sum_s \left(E_k^{\mathrm{CIS}}\delta_{ks} - \boldsymbol{\mu}_{ks}\cdot\boldsymbol{E}(t)\right) c_s(t), \tag{2}$$

where E_k^{CIS} are the HF ($k=0$) and CIS excitation energies, $\boldsymbol{\mu}_{ks} = \langle\Psi_k|\hat{\boldsymbol{\mu}}|\Psi_s\rangle$ are the matrix elements of the dipole moment operator, and $\boldsymbol{\mu}_{ks}\cdot\boldsymbol{E}(t)$ refers to the time-dependent molecule-field interaction. The solution to this equation can be obtained making use of an operator-splitting technique [40, 44]. The time-dependent dipole moment is computed as

$$\boldsymbol{\mu}(t) = \sum_{sk} c_s(t)c_k^*(t)\boldsymbol{\mu}_{ks}, \tag{3}$$

and the HHG spectrum is then obtained as the power spectrum $P(\omega)$

$$P(\omega) = \left|\frac{1}{t_f - t_i}\int_{t_i}^{t_f} W(t)\boldsymbol{\mu}(t)\cdot\hat{\boldsymbol{n}}\; e^{-i\omega t}dt\right|^2, \tag{4}$$

where $\hat{\boldsymbol{n}}$ is the unit vector in the polarization direction, $W(t)$ is the Hann window function and t_i and t_f are, respectively, the initial and the final times for the Fourier transform.

TDSE propagation in presence of an intense external field must account for ionisation, which is modelled in the present work by resorting to the heuristic lifetime model [38].

2.1.1. Rotationally-averaged HHG spectra

In order to simulate the optical response of a randomly oriented molecular systems, we carried out laser-driven electron dynamics with many different polarisation directions of the laser. We used the unit vector $\hat{\mathbf{n}}_s = (\hat{n}_{s,\mathrm{x}}, \hat{n}_{s,\mathrm{y}}, \hat{n}_{s,\mathrm{z}})$ to identify the pulse polarisation direction, where $\hat{n}_{s,\mathrm{x}}$, $\hat{n}_{s,\mathrm{y}}$ and $\hat{n}_{s,\mathrm{z}}$ are random numbers in [-1:1] with the constraint $(\hat{n}_{s,\mathrm{x}}^2+\hat{n}_{s,\mathrm{y}}^2+\hat{n}_{s,\mathrm{z}}^2) \leq 1$.

The rotationally-averaged time-dependent dipole for a molecular fragment labelled with F is computed as

$$\bar{\mu}_{\mathrm{F}}(t) = \frac{1}{S}\sum_s^S \boldsymbol{\mu}_{\mathrm{F}}(t)\cdot\hat{\mathbf{n}}_s, \tag{5}$$

where S is the number of pulse polarisations for a random electric-field polar-

isation $\hat{\mathbf{n}}_s$ and $\boldsymbol{\mu}_{\mathrm{F}}(t)$ is the corresponding time-dependent dipole. Therefore, the averaged HHG spectrum for the fragment F is

$$\bar{P}_{\mathrm{F}}(\omega) = \left| \frac{1}{t_f - t_i} \int_{t_i}^{t_f} W(t) \bar{\mu}_{\mathrm{F}}(t)\ e^{-i\omega t} dt \right|^2. \tag{6}$$

Moreover, we also considered that the experimental sample of the uracil cation upon fragmentation is constituted of various fragments, each of them expected in the sample with a different probability. Therefore, we defined a weighted-averaged time-dependent dipole moment for the sample as

$$\bar{\mu}_{\bar{\mathrm{F}}}(t) = \sum_{\mathrm{F}} \omega_{\mathrm{F}} \bar{\mu}_{\mathrm{F}}(t), \tag{7}$$

where the weights ω_{F} are extracted from the experimental mass spectrum of Hutchison *et al.* [36] and of Lopez-Quintas *et al.* [37].

The HHG spectrum of the weighted-averaged rotationally-averaged time-dependent dipole moment is finally computed as

$$\bar{P}_{\bar{\mathrm{F}}}(\omega) = \left| \frac{1}{t_f - t_i} \int_{t_i}^{t_f} W(t) \bar{\mu}_{\bar{\mathrm{F}}}(t)\ e^{-i\omega t} dt \right|^2. \tag{8}$$

2.1.2. Bound- and continuum-state analysis

Analysing the HHG spectrum in terms of bound- (B) and continuum-state (C) contributions allows one to individuate possible interference effects in the time evolution of the electronic wavefunction [40].

The bound-state contribution to the time-dependent dipole moment of the fragment F is

$$\boldsymbol{\mu}_{\mathrm{F},B}(t) \;=\; \boldsymbol{\mu}_{\mathrm{F},GG}(t) + \sum_{i \in B} \boldsymbol{\mu}_{\mathrm{F},Gi}(t) + \sum_{ij \in B} \boldsymbol{\mu}_{\mathrm{F},ij}(t), \tag{9}$$

while, considering only the continuum states, the time-dependent dipole moment of F is

$$\boldsymbol{\mu}_{\mathrm{F},C}(t) \;=\; \boldsymbol{\mu}_{\mathrm{F},GG}(t) + \sum_{i \in C} \boldsymbol{\mu}_{\mathrm{F},Gi}(t) + \sum_{ij \in C} \boldsymbol{\mu}_{\mathrm{F},ij}(t). \tag{10}$$

In the Equations 9 and 10 $\boldsymbol{\mu}_{\mathrm{F},GG}(t) = |c_0(t)|^2 \boldsymbol{\mu}_{\mathrm{F},00}$ is the ground-ground contribution, $\boldsymbol{\mu}_{\mathrm{F},Gi}(t) = c_0^*(t) c_i(t) \boldsymbol{\mu}_{\mathrm{F},Gi}$ is the ground-excited contribution with the index i running over the bound (B) or continuum (C) states, and $\boldsymbol{\mu}_{\mathrm{F},ij}(t) = c_i^*(t) c_j(t) \boldsymbol{\mu}_{\mathrm{F},ij}$ is the excited-excited contribution with both the

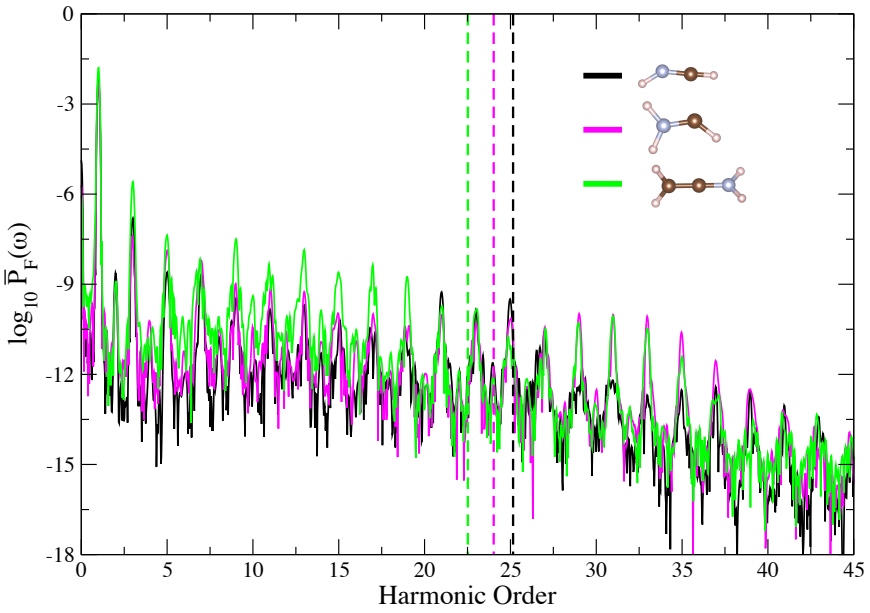

Figure 2: HHG rotationally-averaged spectra of CH_2N^+, $CH_3N^{+\bullet}$ and $C_2H_4N^+$ fragments.

indexes i and j running over the the bound (B) or continuum (C) states. The average of only bound and only continuum time-dependent dipole moment of the fragment is respectively given by

$$\bar{\mu}_{\mathrm{F},B}(t) = \frac{1}{S}\sum_{s}^{S} \boldsymbol{\mu}_{\mathrm{F},B}(t)\cdot\hat{\mathbf{n}}_s \tag{11}$$

and

$$\bar{\mu}_{\mathrm{F},C}(t) = \frac{1}{S}\sum_{s}^{S} \boldsymbol{\mu}_{\mathrm{F},C}(t)\cdot\hat{\mathbf{n}}_s. \tag{12}$$

3. Computational details

The geometry of the uracil cation fragments were taken from the work of Arani *el al.* [53] in which the fragmentation process of the uracil is investigated *via* Density Functional Theory (DFT). The only exception is the OCN^+ fragment which was optimised in its triplet state at HF/cc-pVDZ

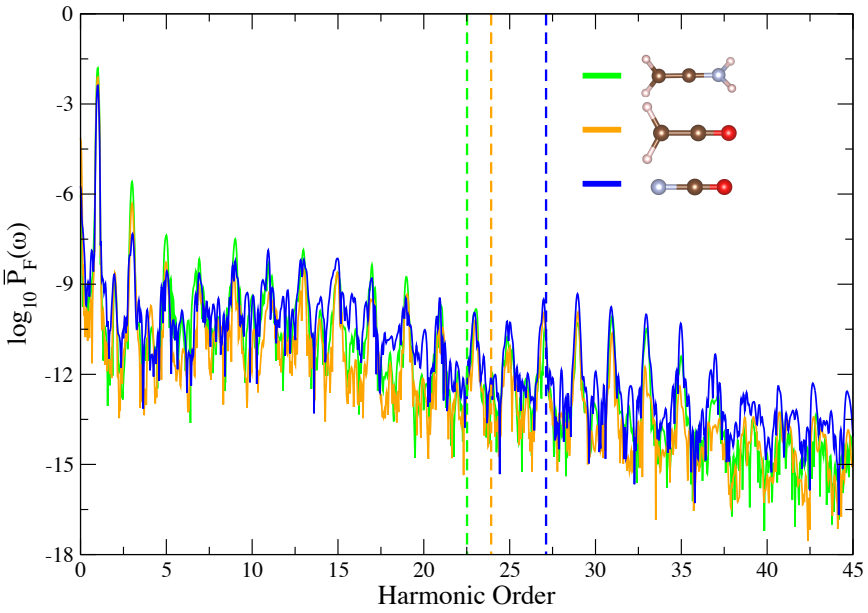

Figure 3: HHG rotationally-averaged spectra of $C_2H_4N^+$, $C_2H_2O^{+\bullet}$ and OCN^+ fragments.

level, using Q-Chem [56]. In fact, using the already optimised DFT geometry from Ref. [53] in combination with optimal-continuum Gaussian basis sets used in the present work led to unphysical convergence of the HF SCF procedure for the CIS calculation.

RT-TD-CIS calculations were performed using the dipole matrix elements and energies from field-free calculations by means of the Q-Chem software package [56], and employed in the homemade code Light [39, 40, 41, 42, 43, 44, 46, 50, 51] that propagates the wavepacket under the influence of a time-dependent field. All results correspond to electronic dynamics at fixed nuclear geometries.

To represent the laser pulse, we have considered an electric field $\mathbf{E}(t)$ polarised along the unit vector $\hat{\mathbf{n}}$

$$\mathbf{E}(t) = E_0 \hat{\mathbf{n}} \sin(\omega_0 t + \phi) f(t), \tag{13}$$

where E_0 is the maximum field strength, ω_0 is the carrier frequency, ϕ is the

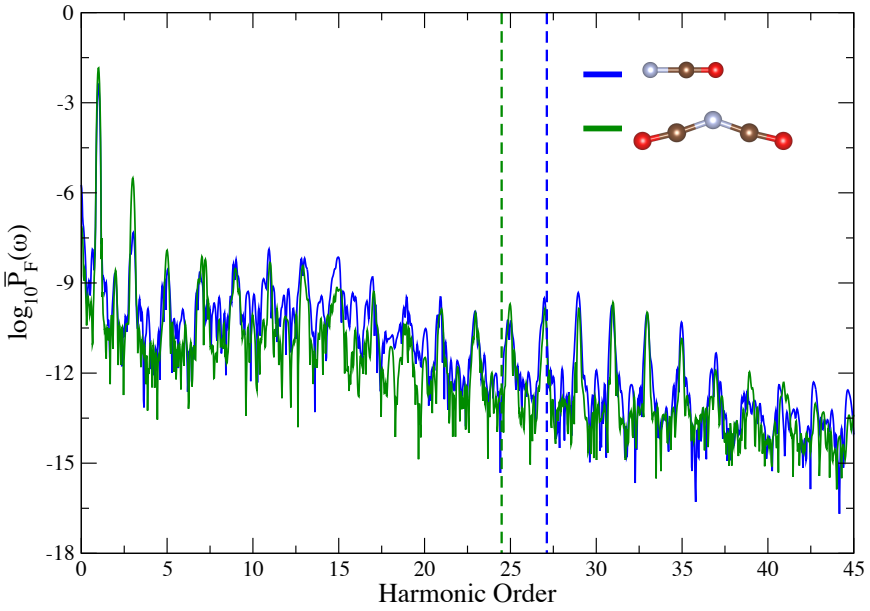

Figure 4: HHG rotationally-averaged spectra of OCN^+ and $C_2NO_2^+$ fragments.

phase and $f(t)$ is the envelope function chosen as

$$f(t) = \begin{cases} \cos^2(\frac{\pi}{2\sigma}(\sigma - t)) & \text{if } |t - \sigma| \leq \sigma, \\ 0 & \text{else.} \end{cases} \tag{14}$$

where σ is the width of the field envelope.

We used the same pulse wavelength of the experiment of Hutchison *et al.* [36], i.e. λ_0 = 780 nm (ω_0=1.59 eV). We used pulse intensities of I = 3×10^{13} W/cm^2 and I = 10^{14} W/cm^2. All the spectra reported here have been calculated with I = 10^{14} W/cm^2 while the spectra calculated with I = 3×10^{13} are reported in the Supplementary Information (SI). The duration of the pulse was 23 optical cycles (oc), where 1 oc = $2\pi/\omega_0$. The time step was 1.21 fs (0.05 a.u.). Value of ionisation energy I_p is taken as minus HOMO energy, following Koopmans theorem. [57] The three-step model (3SM) cutoff used in this work is computed as $1.32I_p$+$3.17U_p$, where U_p is the electron ponderomotive energy. [43, 45, 40, 58, 59, 60]

Concerning the choice of the basis sets, we used the computational strategy developed in the recent years by some of us, which demonstrated to be successful to describe HHG for atomic [43, 46, 32] and molecular species

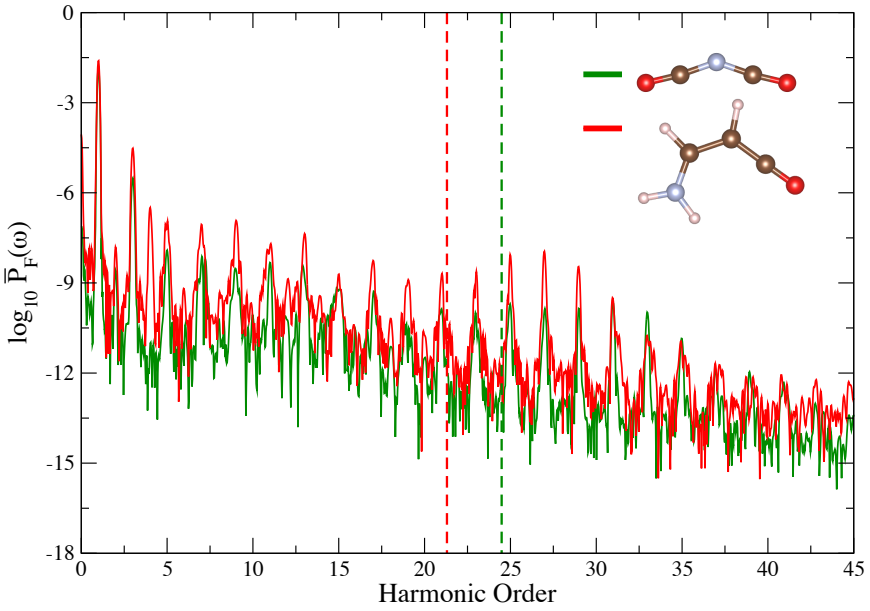

Figure 5: Rotationally-averaged HHG spectra of $C_2NO_2^+$ and $C_3H_4NO^+$ fragments.

[51, 45, 41]. We combined Gaussian continuum functions (K) [61] with the heuristic lifetime model. [38, 43, 46, 32, 45] This model prevents unphysical reflections of the wave function in the laser-driven dynamics. The heuristic lifetime model was originally proposed by Klinkusch *et al.* [38] and it consists of adding to the energies calculated from the field-free Hamiltonian a complex term $\Gamma_k = \sum_{ia} |r^a_{i,k}|^2 \sqrt{2\epsilon_a/d}$ ($\epsilon_a > 0$) which represents the inverse lifetime. The parameter d is empirical representing the characteristic escape length that the electron is allowed to travel during the lifetime $1/\Gamma_k$. According to Refs. [45, 51], the value of d is given by $\frac{E_0}{\omega_0^2}$. A 5aug-cc-pVDZ-3K Gaussian basis set has been used for all the fragments, with the exception of OCN^+, for which the basis set has been reduced to 5aug-cc-pVDZ to overcome convergence issues of the triplet ground state. K functions have been generated using ζ=1 in Eq. 15 of Ref. [61]. Density of states and HHG spectra obtained with $\zeta = 2$ are practically superimposed to the $\zeta = 1$ ones.

The number S of pulse propagation directions was chosen in the 150-350 range, according to the studied fragment. For each fragment, we implemented a convergence study of the HHG spectrum by increasing the number of random orientations. The convergence is achieved when the ratio between odd and even harmonics is high enough to distinguish the physi-

cal signal, and when the shape of the spectrum (intensity and number of harmonics, cutoff region) keeps unchanged with a larger number of random orientations.

4. Results

To compare and analyse the HHG spectra of the different fragments, we followed a *rationale* which correlates the degree of linearity of the fragment with its mass/charge ratio (m/z). This choice follows the idea that starting from physical models, such as Lein model, [62] one can interpret the HHG spectral features from the interference effects between electrons and atoms during the recombination. This is certainly true also in more complex molecules and can be used as criterion of analysis and interpretation of the results. Moroever, we show here only rotationally-averaged HHG spectra in order to compare as close as possible with experimental findings; however, investigating the fragment response to a pulse polarised along its main pseudo-axis could be a valuable tool to understand HHG fine features.

In Figure 2 the HHG rotationally-averaged spectra of the fragments CH_2N^+ (m/z=28), $CH_3N^{+\bullet}$ (m/z=29) and $C_2H_4N^+$ (m/z=42) are shown. The energy cutoff from the 3SM is also shown as a qualitative reference. These are the fragments with the smallest mass/charge ratio and, neglecting the H atoms, are diatomics or linear molecules. It is interesting to observe that fragments CH_2N^+ and $CH_3N^{+\bullet}$ show the same order of magnitude of the peak intensities - before the three-step cutoff - and significantly lower than those of fragment $C_2H_4N^+$; this difference may be caused by the presence of one more carbon atom in $C_2H_4N^+$. Instead, beyond the three-step cutoff, at higher harmonics, the behaviour of CH_2N^+ and $CH_3N^{+\bullet}$ and changes considerably: while peak intensities for CH_2N^+ decrease dramatically , $CH_3N^{+\bullet}$ shows a peak intensity profile similar to $C_2H_4N^+$. As specified above, CH_2N^+ and $CH_3N^{+\bullet}$ differ only for one hydrogen atom, except for which they have the same geometric structure; following the two-interference model [62] they should have the minimum almost at the same position as for the CH_2N^+ the CN bond length is 1.24 Å and for the CH_2N^+ the CN bond length is 1.26 Å. Indeed both fragments share a minimum at the 19th harmonic. The presence of an other hydrogen in fragment $CH_3N^{+\bullet}$ creates an asymmetry, which is reflected in the spatial distribution of electronic orbitals and thus in affecting ionisation and recombination processes, thus leading to a different higher-energy portion of the spectrum. This is translated, at the spectrum level, into a further minimum after the three-step cutoff (25th harmonic), shared with fragment $C_2H_4N^+$, and into the

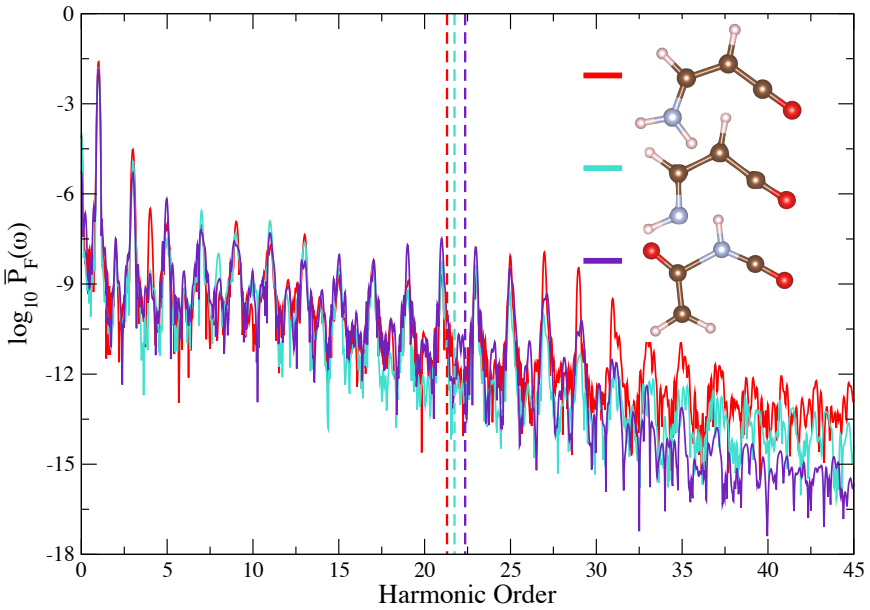

Figure 6: Rotationally-averaged HHG spectra of $C_3H_4NO^+$, $C_3H_3NO^{+\bullet}$ and $C_3H_3NO_2^{+\bullet}$ fragments.

enhancement of HHG peak intensity at high energy.
It is worth mentioning that, though the rotational average typically makes fine features such as minima in the spectrum weaker, our findings are robust against the number of random orientations.

In Figure 3 the HHG rotationally-averaged spectra of the fragments $C_2H_4N^+$, $C_2H_2O^{+\bullet}$ and OCN^+, which all have m/z = 42, are reported. The spectrum for the fragment $C_2H_4N^+$ was already reported in Figure 1. Here, it is considered the reference spectrum with respect to which the HHG spectra of the other fragments should be compared. In this way the differences between the spectra due to the linearity and the m/z ratio are better distinguished.

The general shape of the HHG spectra is very similar for all the fragments. However, the peak intensity of the $C_2H_2O^{+\bullet}$ is lower than the one of the $C_2H_4N^+$ and of the OCN^+. We believe that also in this case an important role is played by the symmetry features of the molecules, which can give rise to different probability concerning ionisation and recombination.

The position of the minimum is at H25 for all the fragments. This can be due to the fact that their molecular skeleton is linear, with similar

interatomic distances, behaving as a three-center interference "generator". [62]

In Figure 4 the rotationally-averaged HHG spectra of OCN^+ (m/z = 42) and $C_2NO_2^+$ (m/z = 70) fragments are shown. The ratio m/z is very different between the two fragments which, however, are characterised by a similar HHG spectrum. The C and O atoms in the $C_2NO_2^+$ are placed in symmetric positions with respect to the N atom. Therefore, the geometry of the $C_2NO_2^+$ is similar to two adjacent OCN^+ moieties. The $C_2NO_2^+$ is the first nonlinear fragment we analyse here. However, the nonlinearity is very small as the CNC angle is around 140°. Therefore, this fragment continues to preserves similar geometrical and orbital symmetry of the OCN^+. However, despite the similarities in the case of the $C_2NO_2^+$ the minimum is shifted lower to the H19 with respect to the H25 of the OCN^+

Figure 5 shows the rotationally-averaged spectra of the fragments $C_2NO_2^+$ and $C_3H_4NO^+$, which have the same m/z = 70. The $C_3H_4NO^+$ is the first fragment in our analysis which geometry is highly nonlinear. However, despite the significant different geometrical arrangement of the atoms, we observe that the position of the minimum does not change with respect the $C_2NO_2^+$, i.e. H19, while the overall intensity of the spectrum is increased. The presence of a strong even harmonics (H4, 6.36 eV) in the $C_3H_4NO^+$ spectrum can be attributed to a system excitation (6.14 eV).

Finally, in Figure 6 the rotationally-averaged spectra of the larger and nonlinear fragments $C_3H_4NO^+$ (m/z = 70), $C_3H_3NO^{+\bullet}$ (m/z = 69) and $C_3H_3NO_2^{+\bullet}$ (m/z = 85) are reported. Comparing the $C_3H_3NO^{+\bullet}$ with the $C_3H_4NO^+$ we observe that the position of the minimum does not change, i.e. H19. Instead, a strong reduction of the harmonic intensity at higher energy (>H27) is found. This reduction is even stronger for the $C_3H_3NO_2^{+\bullet}$ which moreover has the minimum shifted to the H17. The common geometrical feature of these molecules which could influence the ionisation and recombination process is an increasing reduction of the angle opposite to the oxygen on the right. The $C_3H_4NO^+$ has NCC angle = 128°, the $C_3H_3NO^{+\bullet}$ has NCC angle = 115° and finally the $C_3H_3NO_2^{+\bullet}$ CCN angle=112°.

Figures S1-S5 in SI show the same analysis done here when the pulse intensity is equal to $3x10^{13}$ W/cm^2. By comparing corresponding figures at the two pulse intensities, one observes that the minimum is preserved in some cases, and is shifted in other ones. These findings do not allow us at the present stage to clearly state the structural or dynamical nature of such a fine structure.

The interpretation of the HHG spectra of these molecular fragments can be complex because of the interplay of the atomic and many-electron dynam-

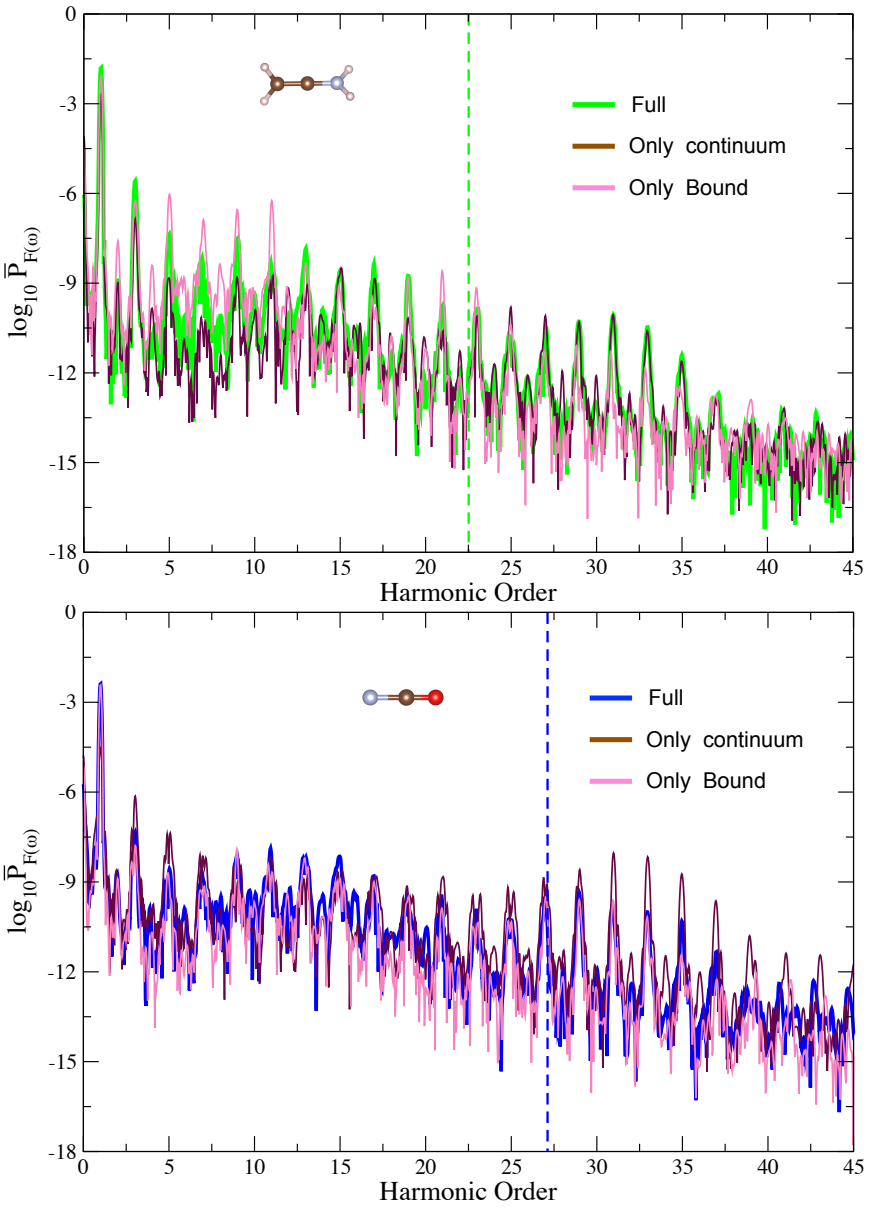

Figure 7: HHG spectra of the C_2NH_4 and OCN^+ fragments compared to the "Only bound" and "Only continuum" HHG spectra of the same fragments.

ics. The geometry plays an important role as well the electron interference between bound and continuum energy states. In Figure 7 we analysed the role of interference between bound and continuum energy states in $C_2H_4N^+$ (upper panel) and OCN^+ (lower panel). We considered these particular fragments because they are representative of a singlet and a triplet spin-state among the fragments of the uracil cation.

We calculated the HHG from the time-dependent dipole moment of Equation 11 which includes only bound states ("Only bound"), and from the time-dependent dipole moment of Equation 12 which includes only continuum states ("Only continuum"). For both the fragments, the continuum energy states are particularly important at high energy while the bound energy states at low energy. [40, 51] However, important differences arise when the two fragments are compared. In fact, for $C_2H_4N^+$ a clear separation of continuum- and bound-state contributions is found: H5-H13 interval in the full spectrum is provided by bound states, which also interfere negatively with the continuum states, since peak intensity for "Only bound" spectrum is higher than that from the "Full" spectrum. In the H27-H35 range, "Full" and "Only continuum" spectra are practically superimposed, indicating a leading contribution in the cutoff region from continuum states. In OCN^+, a negative interference between bound and continuum states is instead found from H25, while in the low- and medium-energy region of the spectrum bound and continuum states contribute at the same extent to the full HHG spectrum.

The analysis of each fragment and the interplay between geometry, electron dynamics and rotational average in the HHG spectrum is necessary to finally characterise the HHG spectrum of the sample made by the all nine fragments studied in this work (see Figure 1). We calculate the HHG spectrum from Equation 8 by calculating the weighted-rotationally-averaged time-dependent dipole moment from Equation 7.

We considered two different sets of weights ω_F in Equation 7. Both sets have been extracted from the intensity of peaks of the mass spectrum of uracil fragmentation. In particular, the first set was obtained from the work of Hutchison *et al.* [36] while the second set was obtained from the work of Lopez *et al.* [37] We reported the normalised sets of weights in Table 1 and in Figure 8 the sample rotationally-averaged HHG spectra together with the rotationally-averaged HHG spectrum of the neutral uracil molecule. Using two different sets of weights does not significantly modify the shape of the weighted-averaged HHG spectrum, even though weights from Lopez *et al.* Ref. [37] produce higher harmonics in the range H19-H31.

Between all the fragments, the CH_2N^+ is the one which is mostly proba-

ble. However, the sample rotationally-averaged HHG spectra in Figure 8 do not resemble that of CH_2N^+ reported in Figure 2. The largest contribution to the sample rotationally-averaged HHG is given by $C_3H_4NO^+$ reported in Figure 5, as one can observe in Figure S6 of SI, where time-dependent dipoles of the fragments are reported.

It is interesting to compare the sample and the single-fragment rotationally-averaged HHG spectra, which are all charged, with the rotationally-averaged HHG spectrum of the neutral uracil molecule [51] (Figure 8). The intensity of the uracil HHG peaks are weaker starting from H20. The charged fragments are characterised by an ionisation potential which is in average 5 eV larger than that of the neutral uracil; for this reason, the high-energy part of the sample HHG spectrum develops towards larger harmonic orders.

5. Conclusions

In the present work we have applied Gaussian-based RT-TD-CIS to fragments of the uracil cation to compute rotationally-averaged HHG spectra in different conditions. We first have grouped the results in terms of structural arrangement of the fragments. For both low and high pulse intensities, similarities in the HHG spectra have been found in the pseudo-diatomics fragments CH_2N^+ and $CH_3N^{+\cdot}$, in the linear and nearly-linear moieties $C_2H_4N^+$, $C_2H_2O^{+\cdot}$, OCN^+ and $C_2NO_2^+$ (with $C_2NO_2^+$ being a kind of "twofold" OCN^+), and in nonlinear fragments $C_3H_4NO^+$, $C_3H_3NO^{+\cdot}$ and $C_3H_3NO_2^{+\cdot}$.

	ω_F from Hutchison *et al.* [36]	ω_F from Lopez-Quintas *et al.*. [37]
CH_2N^+	0.390	0.321
$CH_3N^{+\bullet}$	0.117	0.053
$C_2H_4N^+$	0.130	0.107
$C_2H_2O^{+\bullet}$	0.130	0.107
OCN^+	0.130	0.107
$C_2NO_2^+$	0.013	0.080
$C_3H_4NO^+$	0.013	0.080
$C_3H_3NO^{+\bullet}$	0.039	0.080
$C_3H_3NO_2^{+\bullet}$	0.039	0.064

Table 1: Normalised weights ω_F extracted from the mass spectrum of the uracil fragmentation from Hutchison *et al.* [36] and from Lopez-Quintas *et al.*. [37]

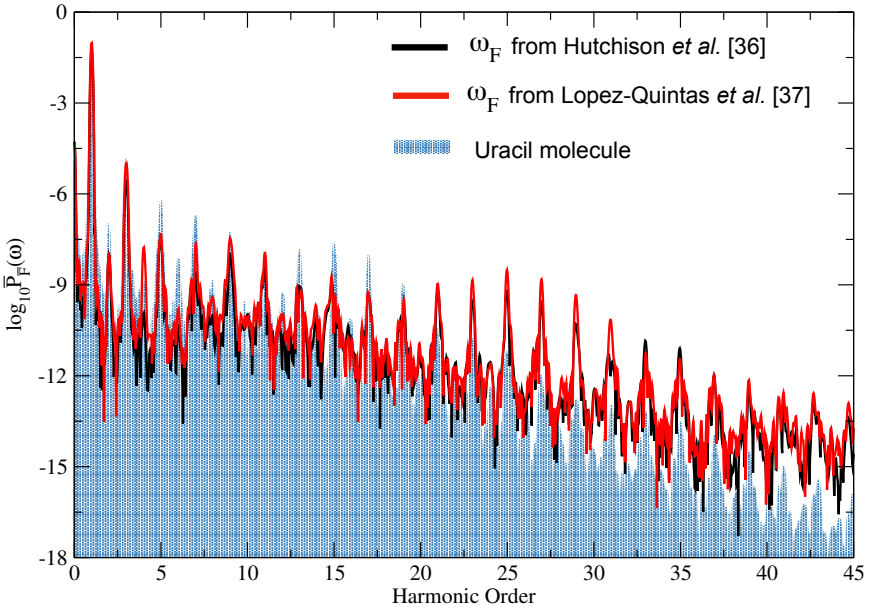

Figure 8: Weighted-rotationally-averaged HHG spectrum for uracil fragments using weights from Hutchison *et al.* [36] and from Lopez-Quintas *et al.* [37] together with the rotationally-averaged HHG spectrum of the neutral uracil molecule.

By decomposing the total time-dependent dipole moment in terms of bound- and continuum-state contributions, we have seen a general behaviour in the analysed fragments, regardless of their geometry, charge or spin state: low-energy (high-energy) harmonics are mainly produced by bound (continuum) states. Differences among the fragments are also observed, especially in the presence for OCN^+ of destructive interference effects between bound- and continuum states.

In order to reduce the gap with the experimental findings we have computed the rotationally-averaged HHG spectrum of the sample, by weighting the fragment contribution according to the peak height in the experimental mass spectrum. What is still missing in our approach is modeling the interaction among fragments and macroscopic propagation effects in the sample.

Our results show that Gaussian-based time-resolved methods can be successfully applied to the investigation of the strong-field electron dynamics on many-electron molecular systems, with different charge and spin states.

Acknowledgements

EC acknowledges funding from University of Trieste via MICROGRANTS 2020.

Supporting Information

Rotationally-averaged HHG spectra of the fragments at I = 3×10^{13} W/cm^2. Rotationally-averaged time-dependent dipoles of the fragments at I = 10^{14} W/cm^2.

References

[1] P. B. Corkum, F. Krausz, Attosecond Science, Nat. Phys. 3 (2007) 381.

[2] F. Krausz, M. Ivanov, Attosecond physics, Rev. Mod. Phys. 81 (2009) 163–234.

[3] S. Haessler, J. Caillat, W. Boutu, C. Giovanetti-Teixeira, T. Ruchon, T. Auguste, Z. Diveki, P. Breger, A. Maquet, B. Carré, R. Taïeb, P. Salières, Attosecond imaging molecular electronic wavepackets, Nature Phys. 6 (2010) 200–206.

[4] S. Baker, I. A. Walmsley, J. W. G. Tisch, J. P. Marangos, Femtosecond to attosecond light pulses from a molecular modulator, Nature Phys. 5 (2011) 664–671.

[5] M. Nisoli, P. Decleva, F. Calegari, A. Palacios, F. Martín, Attosecond Electron Dynamics in Molecules, Chem. Rev. 117 (2017) 10760.

[6] M. Ossiander, F. Siegrist, V. Shirvanyan, R. Pazourek, A. Sommer, T. Latka, A. Guggenmos, S. Nagele, J. Feist, J. Burgdörfer, R. Kienberger, M. Schultze, Attosecond correlation dynamics, Nat. Phys. 13 (2017) 280.

[7] P. Peng, C. Marceau, D. M. Villeneuve, Attosecond imaging of molecules using high harmonic spectroscopy, Nat. Rev. Phys. 1 (2019) 144–155.

[8] G. Sansone, Looking into strong-field dynamics, Nat. Photonics 14 (2020) 131–133.

[9] P. M. Kraus, H. J. Wörner, Perspectives of Attosecond Spectroscopy for the Understanding of Fundamental Electron Correlations, Angew. Chem. Int. Ed. 57 (2018) 5228.

[10] P. M. Kraus, M. Zürch, S. K. Cushing, D. M. Neumark, S. R. Leone, The ultrafast X-ray spectroscopic revolution in chemical dynamics, Nat. Rev. Chem. 2 (2018) 82.

[11] T. T. Gorman, T. D. Scarborough, i. P. M. Abanador, F. Mauger, D. Kiesewetter, i. P. Sándor, S. Khatri, K. Lopata, i. K. J. Schafer, P. Agostini, M. B. Gaarde, L. F. DiMauro, Probing the interplay between geometric and electronic-structure features via high-harmonic spectroscopy, J. Chem. Phys. 150 (2019) 184308.

[12] A. J. Uzan, H. Soifer, O. Pedatzur, A. Clergerie, S. Larroque, B. D. Bruner, B. Pons, M. Ivanov, O. Smirnova, N. Dudovich, Spatial molecular interferometry via multidimensional high-harmonic spectroscopy, Nat. Photonics 14 (2020) 188.

[13] X. Chu, S.-I. Chu, Phys. Rev. A 63 (2001) 023411.

[14] J. Itatani, J. Levesque, D. Zeidler, H. Niikura, H. Ppin, J. C. Kieffer, P. B. Corkum, D. M. Villeneuve, Tomographic imaging molecular orbitals, Nature (London) 432 (2004) 867–871.

[15] L. Cui, J. Zhao, Y. J. Hu, Y. Y. Teng, X. H. Zeng, B. Gu, Effect different laser polarization direction on high order harmonic generation N_2 and H_2, Applied Phys. Lett. 89 (2006) 211103.

[16] S. Patchkovskii, Z. Zhao, T. Brabec, D. M. Villeneuve, High Harmonic Generation and Molecular Orbital Tomography in Multielectron Systems: Beyond the Single Active Electron Approximation, Phys. Rev. Lett. 97 (2006) 123003.

[17] D. A. Telnov, , S.-I. Chu, Effects of multiple electronic shells on strong-field multiphoton ionization and high-order harmonic generation of diatomic molecules with arbitrary orientation: An all-electron time-dependent density-functional approach, Phys. Rev. A 80 (2009) 043412.

[18] O. Smirnova, Y. Mairesse, S. Patchkovskii, N. Dudovich, D. Villeneuve, P. Corkum, M. Y. Ivanov, High harmonic interferometry of multi-electron dynamics in molecules, Nature 460 (2009) 972.

[19] H. J. Wörner, J. Bertrand, P. Hockett, P. Corkum, D. Villeneuve, Controlling the interference of multiple molecular orbitals in high-harmonic generation, Phys. Rev. Lett. 104 (2010) 233904.

[20] S. Sukiasyan, S. Patchkovskii, O. Smirnova, T. Brabec, M. Y. Ivanov, Exchange and polarization effect in high-order harmonic imaging of molecular structures, Phys. Rev. A 82 (2010) 043414.

[21] M. C. H. Wong, J.-P. Brichta, M. Spanner, S. Patchkovskii, V. R. Bhardwaj, High-harmonic spectroscopy of molecular isomers, Phys. Rev. A 84 (2011) 051403(R).

[22] J. Heslar, D. Telnov, S.-I. Chu, High-order-harmonic generation in homonuclear and heteronuclear diatomic molecules: Exploration of multiple orbital contributions, Phys. Rev. A 83 (2011) 043414.

[23] X. Chu, G. C. Groenenboom, Time-dependent density-functional-theory calculation of high-order-harmonic generation of H_2, Phys. Rev. A 85 (2012) 053402.

[24] A. Wardlow, D. Dundas, High-order-harmonic generation in benzene with linearly and circularly polarized laser pulses, Phys. Rev. A 93 (2016) 023428.

[25] P. Mulholland, D. Dundas, High-order harmonic generation from highly-excited states in acetylene, Phys. Rev. A 97 (2017) 43428.

[26] M. Ruberti, P. Decleva, V. Averbukh, Multi-channel dynamics in high harmonic generation of aligned CO_2: *ab initio* analysis with time-dependent B-spline algebraic diagrammatic construction, Phys. Chem. Chem. Phys. 20 (2018) 8311.

[27] C.-T. Le, D.-D. Vu, C. Ngo, V.-H. Le, Influence of dynamic core-electron polarization on the structural minimum in high-order harmonics of CO_2 molecules, Phys. Rev. A 100 (2019) 053418.

[28] B. Wang, Y. He, X. Zhao, L. He, P. Lan, P. Lu, C. D. Lin, Retrieval of full angular-and energy-dependent complex transition dipoles in the molecular frame from laser-induced high-order harmonic signals with aligned molecules, Phys. Rev. A 101 (2020) 63417.

[29] C. Vozzi, M. Negro, F. Calegari, G. Sansone, M. Nisoli, S. D. Silvestri, S. Stagira, Generalized molecular orbital tomography, Nat. Photon. 7 (2011) 822.

[30] P. Saliéres, A. Maquet, S. Haessler, J. Caillat, , R. Taïeb, Rep. Prog. Phys. 75 (2012) 062401.

[31] H. J. Wörner, H. Niikura, J. B. Bertrand, P. B. Corkum, D. M. Villeneuve, Observation of Electronic Structure Minima in High-Harmonic Generation, Phys. Rev. Lett. 102 (2009) 103901.

[32] E. Coccia, How electronic dephasing affects high-harmonic generation in atoms, Mol. Phys. 118 (2020) e1769871.

[33] D. R. Tuthill, F. Mauger, T. D. Scarborough, R. R. Jones, M. B. Gaarde, K. Lopata, K. J. Schafer, L. F. DiMauro, Multidimensional molecular high-harmonic spectroscopy: A road map for charge migration studies, J. Mol. Spectrosc. 372 (2020) 111354.

[34] W. Li, X. Zhou, R. Lock, S. Patchkovskii, A. Stolow, H. C. Kapteyn, M. M. Murnane, Time-Resolved Dynamics in N_2O_4 Probed Using High Harmonic Generation, Science 322 (2008) 1207.

[35] J. Marangos, Development of high harmonic generation spectroscopy of organic molecules and biomolecules, J. Phys. B 49 (2016) 132001.

[36] C. Hutchison, R. Ganeev, M. Castillejo, I. Lopez-Quintas, A. Zair, S. Weber, F. McGrath, Z. Abdelrahman, M. Oppermann, M. Martin,

D. Lei, S. Maier, J. Tisch, J. Marangos, Comparison of high-order harmonic generation in uracil and thymine ablation plumes, Phys. Chem. Chem. Phys. 15 (2013) 12308–12313.

[37] I. Lopez-Quintas, M. Oujja, M. Sanz, A. B.-C. nete, C. Hutchison, R. de Nalda, M. Martin, R. A. Ganeev, J. Marangos, M. Catillejo, Characterization of laser-induced plasmas of nucleobases: Uracil and thymine, Appl. Surf. Sci. 302 (2014) 299.

[38] S. Klinkusch, P. Saalfrank, T. Klamroth, Laser-induced electron dynamics including photoionization: A heuristic model within time-dependent configuration interaction theory, J. Chem. Phys. 131 (2009) 114304.

[39] E. Luppi, M. Head-Gordon, Computation high-harmonic generation spectra H_2 and N_2 in intense laser pulses using quantum chemistry methods and time-dependent density functional theory, Mol. Phys. 110 (2012) 909.

[40] E. Luppi, M. Head-Gordon, Role of Rydberg and continuum levels in computing high harmonic generation spectra the hydrogen atom using time-dependent configuration interaction, J. Chem. Phys. 139 (2013) 164121.

[41] A. White, C. J. Heide, P. Saalfrank, M. Head-Gordon, E. Luppi, Computation of high-harmonic generation spectra of the hydrogen molecule using time-dependent configuration-interaction, Mol. Phys. 114 (2016) 947.

[42] E. Coccia, E. Luppi, Optimal-continuum and multicentered Gaussian basis sets for high-harmonic generation spectroscopy, Theor. Chem. Acc. 135 (2016) 43.

[43] E. Coccia, B. Mussard, M. Labeye, J. Caillat, R. Taïeb, J. Toulouse, E. Luppi, Gaussian continuum basis functions for calculating high-harmonic generation spectra, Int. J. Quant. Chem. 116 (2016) 1120.

[44] E. Coccia, R. Assaraf, E. Luppi, J. Toulouse, *Ab initio* lifetime correction to scattering states for time-dependent electronic-structure calculations with incomplete basis sets , J. Chem. Phys. 147 (2017) 014106.

[45] M. Labeye, F. Zapata, E. Coccia, V. Veniard, J. Toulouse, J. Caillat, R. Taïeb, E. Luppi, Optimal Basis Set for Electron Dynamics in Strong

Laser Fields: The case of Molecular Ion H_2^+, J. Chem. Theory Comput. 14 (2018) 5846.

[46] E. Coccia, E. Luppi, Detecting the minimum in argon high-harmonic generation spectrum using Gaussian basis sets, Theor. Chem. Acc. 138 (2019) 96.

[47] F. Bedurke, T. Klamroth, P. Krause, P. Saalfrank, Discriminating organic isomers by high harmonic generation: A time-dependent configuration interaction singles study, J. Chem. Phys. 150 (2019) 234114.

[48] P. Saalfrank, F. Bedurke, C. Heide, T. Klamroth, S. Klinkusch, P. Krause, M. Nest, J. C. Tremblay, Molecular attochemistry: Correlated electron dynamics driven by light, Adv. Quant. Chem. 81 (2020) 15.

[49] M. K. Lee, W. Li, H. B. Schlegel, Angular dependence of strong field sequential double ionization for neon and acetylene simulated with time-dependent configuration interaction using CIS and CISD-IP, J. Chem. Phys. 152 (2020) 064106.

[50] C. F. Pauletti, E. Coccia, E. Luppi, J. Chem. Phys. 154 (2021) 014101.

[51] E. Luppi, E. Coccia, Probing the molecular frame of uracil and thymine with high-harmonic generation spectroscopy, Phys. Chem. Chem. Phys. 23 (2021) 3729.

[52] F. Bedurke, T. Klamroth, P. Saalfrank, Many-electron dynamics in laser-driven molecules: wavefunction theory vs. density functional theory, Phys. Chem. Chem. Phys. 23 (2021) 13544.

[53] L. S. Arani, P. Mignon, H. Abdoul-Carime, B. Farizon, M. Farizon, H. Chermette, DFT study of the fragmentation mechanism of uracil RNA base, Phys. Chem. Chem. Phys. 14 (2012) 9855.

[54] A. Dreuw, M. Head-Gordon, Single-Reference ab Initio Methods for the Calculation Excited States Large Molecules, Chem. Rev. 105 (2005) 4009–4037.

[55] E. Coccia, E. Luppi, Time-dependent ab initio approaches for high-harmonic generation spectroscopy, Journal of Physics: Condensed Matter 34 (2021) 073001. URL: https://doi.org/10.1088/1361-648x/ac3608. doi:10.1088/1361-648x/ac3608.

[56] Y. Shao, L. F. Molnar, Y. Jung, J. r. Kussmann, C. Ochsenfeld, S. T. Brown, A. T. B. Gilbert, L. V. Slipchenko, S. V. Levchenko, D. P. O Neill, R. A. DiStasio Jr, R. C. Lochan, T. Wang, G. J. O. Beran, N. A. Besley, J. M. Herbert, C. Yeh Lin, T. Van Voorhis, S. Hung Chien, A. Sodt, R. P. Steele, V. A. Rassolov, P. E. Maslen, P. P. Korambath, R. D. Adamson, B. Austin, J. Baker, E. F. C. Byrd, H. Dachsel, R. J. Doerksen, A. Dreuw, B. D. Dunietz, A. D. Dutoi, T. R. Furlani, S. R. Gwaltney, A. Heyden, S. Hirata, C.-P. Hsu, G. Kedziora, R. Z. Khaliullin, P. Klunzinger, A. M. Lee, M. S. Lee, W. Liang, I. Lotan, N. Nair, B. Peters, E. I. Proynov, P. A. Pieniazek, Y. Min Rhee, J. Ritchie, E. Rosta, C. David Sherrill, A. C. Simmonett, J. E. Subotnik, H. Lee Woodcock III, W. Zhang, A. T. Bell, A. K. Chakraborty, D. M. Chipman, F. J. Keil, A. Warshel, W. J. Hehre, H. F. Schaefer III, J. Kong, A. I. Krylov, P. M. W. Gill, M. Head-Gordon, Advances in methods and algorithms in a modern quantum chemistry program package, Phys. Chem. Chem. Phys. 8 (2006) 3172.

[57] A. Szabo, N. S. Ostlund, Modern Quantum Chemistry, MacMillan, 1982.

[58] M. Lewenstein, P. Balcou, M. Y. Ivanov, A. L'Huillier, P. B. Corkum, Theory of high-harmonic generation by low-frequency laser fields, Phys. Rev. A 49 (1994) 2117.

[59] P. B. Corkum, Plasma perspective on strong field multiphoton ionization, Phys. Rev. Lett. 71 (1993) 1994.

[60] J. L. Krause, K. J. Schafer, K. C. Kulander, Calculation of photoemission from atoms subject to intense laser fields, Phys. Rev. A 45 (1992) 4998.

[61] K. Kaufmann, W. Baumeister, M. Jungen, Universal Gaussian basis sets for an optimum representation Rydberg and continuum wavefunctions, J. Phys. B: At. Mol. Opt. Phys. 22 (1989) 2223.

[62] M. Lein, N. Hay, R. Velotta, J. P. Marangos, P. L. Knight, Interference effects in high-order harmonic generation with molecules, Phys. Rev. A 66 (2002) 023805.